Chemical Science

ROYAL SOCIETY OF CHEMISTRY

EDGE ARTICLE

View Article Online
View Journal

Cite this: DOI: 10.1039/d5sc07537h

All publication charges for this article have been paid for by the Royal Society of Chemistry

Curvature defect engineering towards a high-performance COF-based cathode in lithium-ion batteries

Ju Duan, Haojie Zhou, Wenxiao Bi, Jiawei Liu, Linchu Xu, Weisi He, Xinyuan Sun, Huawei Hu, Wei Lyu * and Yaozu Liao *

Covalent organic frameworks (COFs), a type of function-oriented porous material, show great potential in rechargeable batteries owing to well-defined ion channels and a flexible framework design. However, the active sites in COFs are almost impossible to fully utilize because of insufficient electron transport or ion diffusion. Here, a defect-rich COF@CNT cathode (RBT-COF@CNT-50) was designed using curvature defect engineering to enhance the electrochemical reaction kinetics. The synergistic effect of the defect-rich D–A framework with the CNT-interlaced network endows RBT-COF@CNT-50 with a higher electron conductivity of 2.65 × 10^{-4} S m^{-1}. The emergence of additional defect decorated with polar functional groups in RBT-COF@CNT, induced by the curvature effects, contributes to faster ion diffusion. Consequently, RBT-COF@CNT-50 delivers a higher reaction rate of 1.22 × 10^{-6} mol s^{-1} m^{-2}. As expected, RBT-COF@CNT-50 reveals a high specific capacity of 302 mAh g^{-1} at 0.1 A g^{-1}. It also exhibits excellent long-term cycling performance with 148 mA g^{-1} at 2 A g^{-1} for 2000 continuous cycles and 124 mA g^{-1} with a capacity attenuation rate of 0.004% per cycle at 10 A g^{-1}, outperforming most reported COF/carbon composite cathodes. This work offers in-depth insights into the construction of high-performance COF-based cathodes by enhancing electrochemical reaction kinetics with curvature defect engineering.

Received 29th September 2025
Accepted 16th December 2025

DOI: 10.1039/d5sc07537h

rsc.li/chemical-science

Introduction

The use of lithium-ion batteries (LIBs), as an emerging technological innovation, has increased at an astonishing rate throughout society, driving the widespread adoption of equipment using renewable energy, including portable electronic devices, electric vehicles, and aerospace applications.[1–3] Nevertheless, the rapidly increasing demand for LIBs presents significant challenges in designing cathode materials to overcome theoretical capacity limitations.[4,5] In contrast to conventional inorganic cathode materials, organic cathode materials have attracted extensive attention owing to their sustainability, cost-effectiveness, and structural design flexibility.[6–8] Among them, covalent organic frameworks (COFs), crystalline porous materials linked by robust covalent bonds, represent a pioneering material platform that aligns precisely with functional requirements. Their unique features, including well-defined open channels, tunable chemical properties, and large specific surface areas, endow COFs with great potential for energy storage.[8,9] However, optimizing electrochemical reaction kinetics within COFs remains crucial for achieving excellent electrochemical performance.

According to the "wiring lengths" concept: $L_e/L_{ions} = (\sigma_e/\sigma_{ions})^{1/2}$, the ion diffusion length (L_{ions}) and electron conduction length (L_e) should be matched to ensure high accessibility of active sites, accompanied by high electron conductivity (σ_e) and ion conductivity (σ_{ions}).[10,11] Therefore, optimizing electrochemical reaction kinetics requires improvements in both electron conduction and ion diffusion. On the one hand, various structural design strategies have been explored to enhance electron transport, including metal ion coordination,[12] extended conjugated electron delocalization,[13] and donor–acceptor (D–A) mediated electron transport.[14] In particular, COF/carbon composite materials have proven to be effective, leveraging the excellent electron-donating properties of carbon materials through π–π interactions.[15] On the other hand, although COFs naturally possess well-defined pores that favor ion diffusion, the ion solvation structure inside organic electrodes, unlike that in inorganic electrodes, remains a critical factor influencing reaction kinetics.[16] Several approaches have been proposed to regulate solvation structures, such as introducing polar groups,[17] modifying framework charges,[16] and employing solvent additives.[18] Among these, tailoring the framework polarity is regarded as a convenient and versatile strategy due to the inherent structural diversity of COFs.[17]

State Key Laboratory of Advanced Fiber Materials, College of Materials Science and Engineering, Donghua University, Shanghai 201620, China. E-mail: wlyu@dhu.edu.cn; yzliao@dhu.edu.cn

Nevertheless, achieving simultaneous improvements in electron transport and ion diffusion still represents a significant challenge.

Structural defects, which are inevitably generated during COF synthesis, have been shown to strongly influence electron conduction and ion diffusion.[19,20] Vacancy defects are reported to enhance electron conductivity by introducing additional energy levels around the Fermi level.[19] Notably, vacancy defects may form during COF growth which will be further generated due to the curvature effect of carbon nanotubes (CNTs).[21] In addition, vacancy defects will endow the framework structure with more regulation in the solvation structure, further influencing the ion diffusion.[17] Hence, rationally designing COF/carbon composite materials provides an effective pathway for achieving high performance with optimized electrochemical reaction kinetics.

Herein, we designed a defect-rich COF@CNT cathode material (RBT-COF@CNT-50) with a core–shell structure *via* curvature defect engineering, using CNTs as templates to optimize electrochemical reaction kinetics. The CNTs act as highly conductive cores, providing efficient electron transport pathways, while the covering defect-rich donor–acceptor (D–A) type COF (RBT-COF) shell offers high porosity and abundant active sites. This defect-rich D–A framework on the surface of the CNTs enables better electron transport with markedly enhanced electronic conductivity for RBT-COF@CNT-50 (2.65×10^{-4} S m^{-1}) compared to pristine BT-COF (3.16×10^{-14} S m^{-1}). In addition, more defects promoted by the curvature-induced effect facilitate faster ion diffusion. As a result, RBT-COF@CNT-50 achieves a significantly higher reaction rate (1.22×10^{-6} mol s^{-1} m^{-2}) compared with both BT-COF (0.85×10^{-6} mol s^{-1} m^{-2}) and physical mixing of BT-COF with 50 wt% CNTs (BT-COF/CNT-50, 0.97×10^{-6} mol s^{-1} m^{-2}). As expected, RBT-COF@CNT-50 reveals a high specific capacity of 302 mAh g^{-1} at 0.1 A g^{-1}. It also displays excellent long-term cycling performance at 2 A g^{-1} with 148 mA g^{-1} even after 2000 cycles. When further increased to 10 A g^{-1}, RBT-COF@CNT-50 still delivers a high initial discharge specific capacity of 124 mA g^{-1} with a capacity attenuation rate of 0.004% per cycle, outperforming most reported COF/carbon composite cathodes. This work demonstrates a facile yet effective strategy to enhance electrochemical reaction kinetics, offering valuable insights into the development of advanced nanofiber porous cathodes for high-performance energy storage applications.

Results and discussion

In this work, leveraging single-walled carbon nanotubes (CNTs) as structural templates, we engineered a core–shell architecture (denoted as RBT-COF@CNT) through *in situ* growth with a tris(4-aminophenyl)amine motif (TPA, electron donor) as a p-type monomer reacting with a benzoterthiophene motif (BTT, electron acceptor), promoting optimized electron transport *via* π–π interfacial interactions as shown in Fig. 1a (see SI for details).[22] The crystalline structure was validated by powder X-ray diffraction (PXRD) patterns, revealing an AA stacking mode refined by Pawley fitting using Materials Studio (Fig. 1b and Table S1). The PXRD pattern of BT-COF closely matches the simulated AA stacking model, exhibiting low R_p (3.50%) and R_{wp} (2.57%). The ternary structure of TPA imparts BT-COF with a larger interlayer spacing of 4.09 Å. Upon CNT incorporation, the crystallinity is preserved with reduced diffraction intensity, particularly at 50 wt% CNT loading (RBT-COF@CNT-50, Fig. S1a). A distinct peak at ~26.1°, corresponding to the (002) lattice plane of CNTs, is also observed.[23,24]

The chemical structure of RBT-COF was further verified by Fourier-transform infrared spectroscopy (FT-IR, Fig. 1c and S1b). The disappearance of N–H stretching (~3200–3500 cm^{-1}) from TPA, the reduction of the C=O band (1658 cm^{-1}) from BTT, and the appearance of an imine peak (C=N, 1607 cm^{-1}) collectively confirm the formation of BT-COF.[8] Solid-state ^{13}C CP/MAS nuclear magnetic resonance (^{13}C NMR) spectra (Fig. S1c) display characteristic peaks of the COF backbone, which broaden upon CNT addition owing to sideband effects arising from the high conductivity of CNTs.[25] Increasing the CNT content results in the gradual emergence of aldehyde groups alongside weakened imine bonds, suggesting that CNTs may influence polymerization and induce the generation of additional vacancy defects. X-ray photoelectron spectroscopy (XPS, Fig. S1d and e) further supports this result with O 1s spectra, indicating increased defect concentration in RBT-COF formed on the CNT surfaces. More framework defects accompanied by a gradually increasing CNT proportion can be further verified by electron paramagnetic resonance (EPR) spectra in Fig. S1d. One pair of sign peaks located at ~3510 G can be observed, which represents the triphenylamine radicals in BT-COF.[26] When the CNT addition increases to 10 wt%, this characteristic signal peak increases, which could be because of enhanced dispersion of COF crystals.[27] Following the further increase of the CNT addition proportion to 30% and 50%, the signal peak intensity gradually weakens, suggesting that the triphenylamine radicals decline with more framework defects. This phenomenon indicates that the number of defects increases with the addition of CNTs. However, BT-COF/CNT-50 shows no characteristic signal peaks, which is attributed to the electromagnetic shielding effect generated by a high proportion of CNTs with a conductive network.[28] Moreover, peak shifts of C=N from 1607 to 1602 cm^{-1} and C=O from 1669 to 1662 cm^{-1} demonstrate strong π–π interfacial interactions between RBT-COF and CNTs. This interaction is also evident in physical mixing between BT-COF and 50 wt% CNT (BT-COF/CNT-50).[29,30] Raman spectroscopy reveals distinct G′ bands associated with out-of-plane carbon vibrations in CNTs (Fig. 1d), with the intensity progressively increasing from 10 to 50 wt% CNT (Fig. S1f). A slight shift in the G band (from 1578 cm^{-1} in BT-COF to 1583 cm^{-1} in BT-COF/CNT-50 and RBT-COF@CNT-50) further evidences π–π interactions between CNTs and BT-COF.[29]

N_2 isothermal adsorption/desorption measurements were conducted to evaluate the Brunauer–Emmett–Teller (BET) surface area (S_{BET}) of RBT-COF with different addition contents of CNTs, as shown in Fig. 1e and S2a. Pristine BT-COF exhibits a high S_{BET} of 701 m^2 g^{-1}, which decreases to 426, 308, and 286 m^2 g^{-1} with increasing CNT content (10, 30, and 50 wt%,

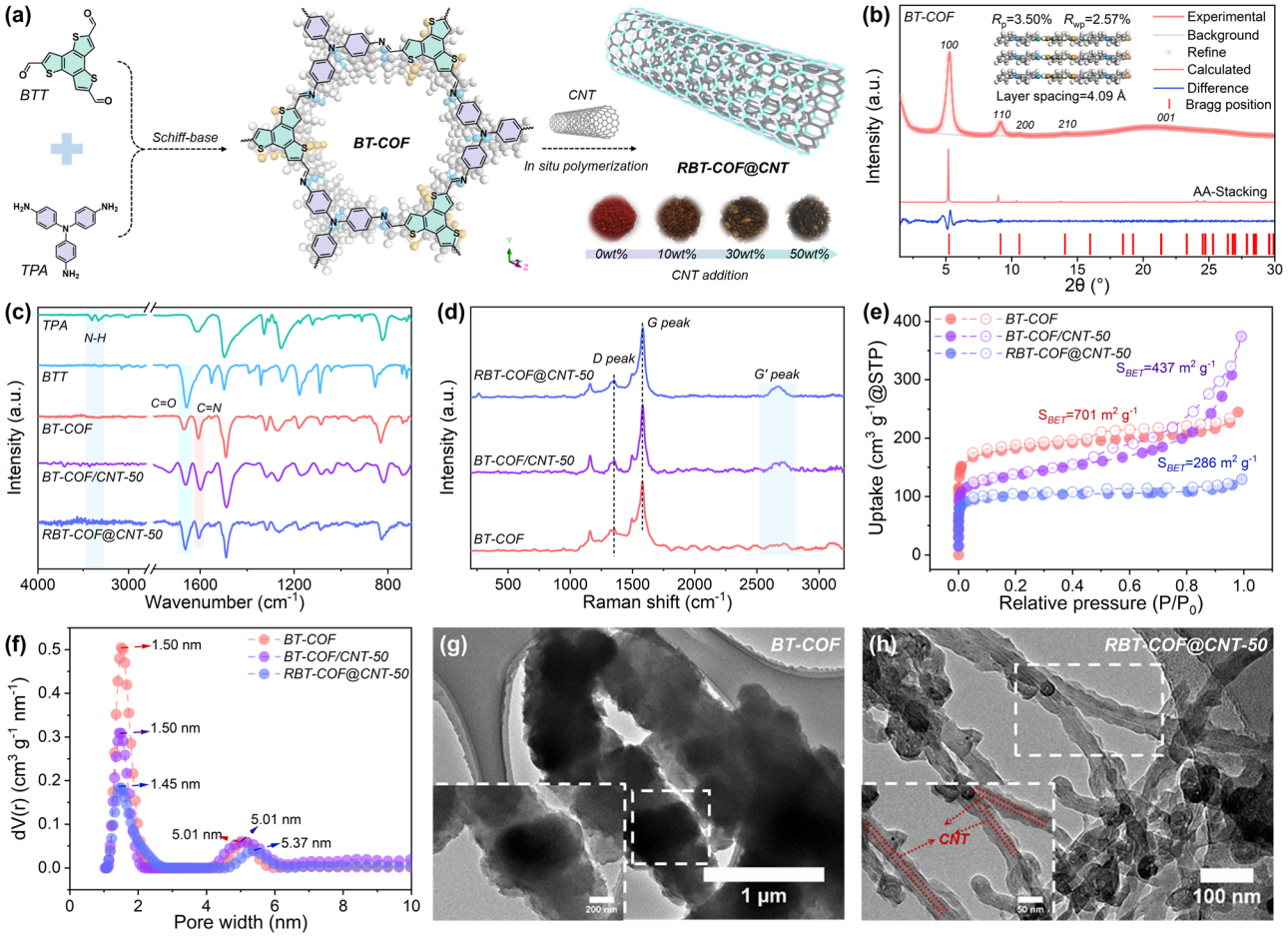

Fig. 1 (a) A schematic diagram of BT-COF and RBT-COF@CNT. (b) The PXRD patterns of BT-COF with AA stacking and Pawley-refinement. (e) N_2 isothermal adsorption/desorption curves with (f) pore-size distribution and (d) Raman spectra for BT-COF, BT-COF-CNT-50, and RBT-COF@CNT-50. (c) FT-IR spectra of BT-COF and RBT-COF@CNT-50 with the related monomers. TEM images with local selection amplification for (g) BT-COF and (h) RBT-COF@CNT-50.

respectively), attributable to the relatively low surface area of CNTs (334 $m^2\ g^{-1}$, Fig. S2b). The pore-size distribution, calculated by non-local density functional theory (NLDFT, Fig. 1f and S2c), shows that BT-COF possesses a dominant pore size of 1.50 nm, which slightly decreases to 1.45 nm in RBT-COF@CNT-50 due to layer interlacing and stacking disorder (consistent with PXRD in Fig. S1a).[31] Notably, the total pore volume significantly decreases, shortening the ion diffusion pathway. Additionally, BT-COF displays a mesopore size (5.01 nm) arising from interparticle voids. This mesopore size expands to 5.37 nm in RBT-COF@CNT-50, likely due to improved dispersion of COF nanocrystals by CNT incorporation. A similar reduction in S_{BET} (437 $m^2\ g^{-1}$) and a nearly identical pore-size distribution are observed for BT-COF/CNT-50 compared to BT-COF.

Morphological analysis *via* scanning electron microscopy (SEM, Fig. S3a) shows that BT-COF adopts a rod-like morphology composed of aggregated nanocrystals. In contrast, RBT-COF@CNT evolves into a uniform nanofibrous structure with improved COF dispersion as the CNT loading increases (Fig. S3b–d). Transmission electron microscopy (TEM, Fig. 1g, h, and S4) further confirms this transformation. Pristine BT-COF forms thick nanocrystalline aggregates (>200 nm), limiting active site accessibility. Meanwhile, the average thickness of the BT-COF shell on the surface of the CNTs decreases to ~130, ~80, and ~40 nm, respectively, with the CNT content increasing to 10 wt%, 30 wt%, and 50 wt%, enabling higher surface active site exposure and shortened ion diffusion distances.[32] The reduction in domain sizes for the COF with increasing CNT proportion might be because of the presence of more heterogeneous nucleation sites based on the strong π–π interaction between the COF and CNTs.[15] Elemental mapping based on energy-dispersive X-ray spectroscopy (EDS, Fig. S5) indicates a homogeneous distribution of C, N, S, and O across the CNT surface. Thermogravimetric analysis (TGA, Fig. S6) verifies the RBT-COF content in RBT-COF@CNT-50 (~56%), consistent with the theoretical composition and confirming the material accuracy.

To gain deeper insights into the influence of CNTs on the polymerization of BT-COF, density functional theory (DFT) calculations were performed at the B3LYP/6-31G(d) level. Upon CNT introduction, the spatial configuration of BT-COF changes

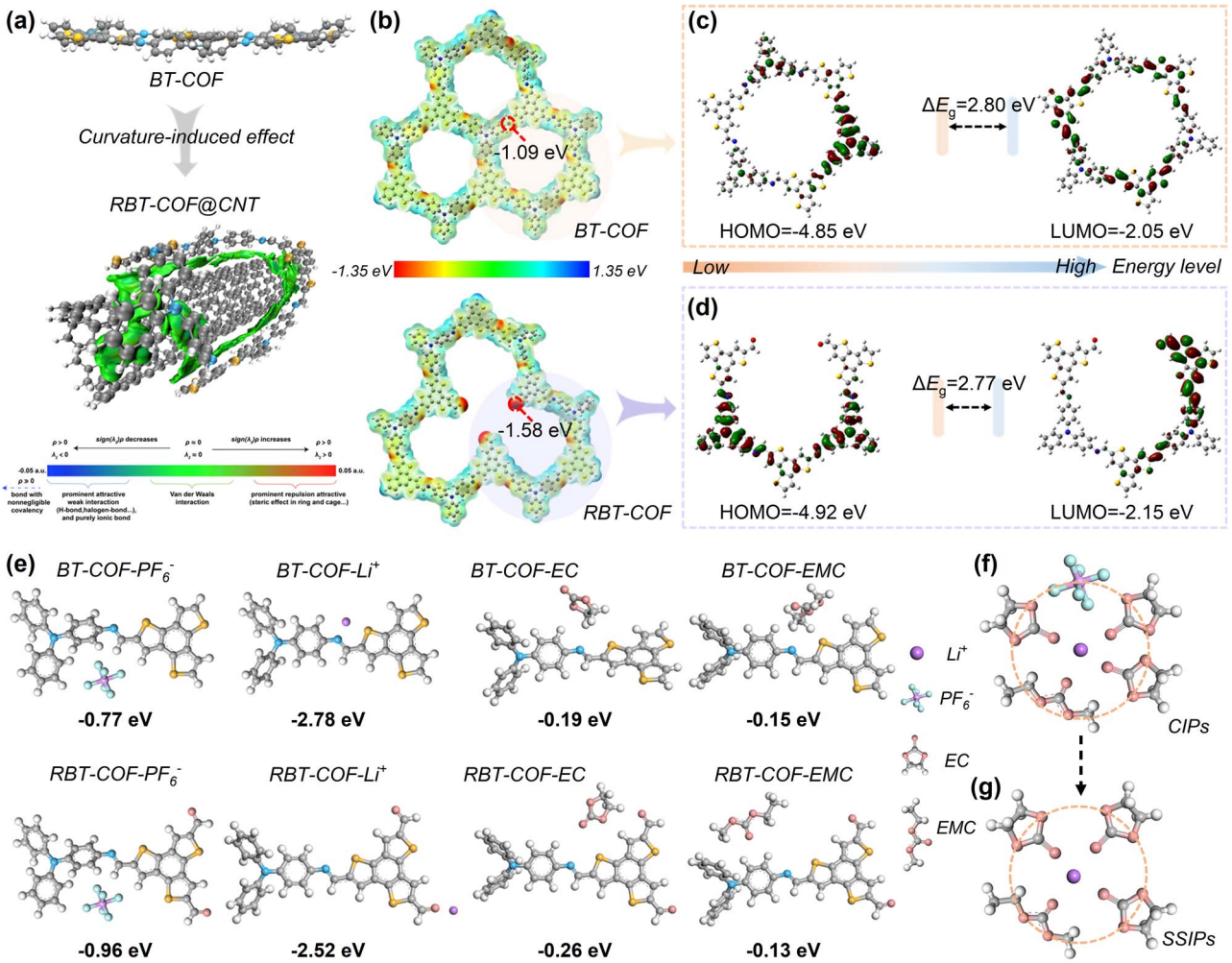

Fig. 2 (a) A representation of the structural change from BT-COF to RBT-COF@CNT and weak interaction regions visualized with a δ_g^{inter} isovalue of 0.005 a.u. in the IGMH analysis for RBT-COF@CNT. (b) MESP of BT-COF and RBT-COF. The HOMO and LUMO energy levels with the energy gap of the structural units for (c) BT-COF and (d) RBT-COF. (e) The binding energies of BT-COF and RBT-COF with different electrolyte compositions. The solvation structure in (f) BT-COF and (g) RBT-COF.

from a planar to a curved surface due to substrate curvature effect (Fig. 2a). The formation of the unique core–shell architecture in BT-COF@CNT is primarily attributed to π–π interactions between the BT-COF framework and CNTs, as indicated by the independent gradient model based on Hirshfeld partition (IGMH) analysis (Fig. 2a).[24,33] This curvature-induced configuration disrupts framework stacking, thereby generating additional defects in the RBT-COF shell as CNT loading increases. Importantly, the strong π–π interaction also facilitates electron transport by coupling with the intrinsic high electron conductivity of CNTs.[32]

The defect-rich nature of the BT-COF shell was further evaluated by molecular electrostatic potential (MESP) mapping (Fig. 2b). As a comparison, the formyl group exhibits a lower electrostatic potential (−1.58 eV) than the imine group (−1.09 eV), suggesting that defects in RBT-COF more readily coordinate cations from the electrolyte. Moreover, the average MESP value of RBT-COF (−0.21 kcal mol^{-1}) is higher than that of BT-COF (−0.46 kcal mol^{-1}), owing to the loss of one electron-donating TPA unit. More electron-deficient characteristics of RBT-COF enhance anion interaction from the electrolyte.[16] The improved electron transport properties of RBT-COF are further supported by the highest occupied molecular orbital-lowest unoccupied molecular orbital (HOMO–LUMO) energy level gaps (ΔE_g, Fig. 2c and d). The RBT-COF framework exhibits a narrower HOMO–LUMO gap (2.77 eV) compared with BT-COF (2.80 eV), arising from a reduced LUMO energy from −2.15 to −2.05 eV. The HOMO and LUMO levels are evenly distributed on the TPA (donor) and BTT (acceptor) units, establishing an efficient D–A electron transport pathway. This arrangement facilitates electron transport from TPA to BTT and simultaneously enhances the ion–framework interaction, thereby improving active site accessibility.[16] In summary, DFT calculations confirm that the unique core–shell RBT-COF@CNT-50 architecture provides dual benefits in enhancing electron transport and defect-inducing active-site formation.

The better electron transport ability of RBT-COF@CNT-50 was further experimentally validated. UV-vis diffuse

reflectance spectra (DRS, Fig. S7a) were used to calculate optical energy gaps (Fig. S7b). RBT-COF@CNT-50 exhibits a narrower energy gap (1.63 eV) compared to BT-COF (1.92 eV) and BT-COF/CNT-50 (1.79 eV), consistent with enhanced electron transport. Furthermore, the electron conductivity (σ_e) of RBT-COF@CNT-50 reaches 2.65×10^{-4} S m^{-1} (Fig. S8a), markedly higher than that of BT-COF (3.16×10^{-14} S m^{-1}) and comparable to that of BT-COF/CNT-50 (8.04×10^{-4} S m^{-1}, Fig. S8b) based on eqn (S1). These results, in agreement with theoretical predictions, highlight the promoted electron transport by the defect effect for RBT-COF and π–π interactions with CNTs.

Unlike inorganic electrode materials, ion diffusion in organic frameworks is strongly influenced by solvation structures.[34] The charge density change of the framework can affect the solvation structure inside the COF, promoting transport and dissociation.[35] Defects within the framework play a critical role in regulating these ion diffusion structures, as revealed by binding energy calculations between COFs and electrolyte components (Fig. 2e). RBT-COF shows stronger binding in TPA with PF_6^- (−0.96 eV) and BTT with EC (−0.26 eV) compared with BT-COF (−0.77 and −0.19 eV, respectively), reflecting its more electron-deficient characteristics. This stronger anion-framework interaction promotes a transformation in the solvation structure from predominantly contact ion pairs (CIPs, Fig. 2f) toward solvent-separated ion pairs (SSIPs, Fig. 2g), thereby accelerating ion diffusion within RBT-COF.[16,36] Raman spectroscopy further confirms this transformation, as shown in Fig. S9. The proportion of coordinated PF_6^- decreases from 63% to 55%, accompanied by an increase in free PF_6^-, indicating a higher transformation proportion of SSIPs. Such defect-induced solvation regulation enables faster ion diffusion, which is expected to result in superior electrochemical kinetics of RBT-COF@CNT-50.

To investigate the effect of enhanced electron and ion transport on electrochemical performance, BT-COF, BT-COF/CNT-50, and RBT-COF@CNT-50 were evaluated as cathodes for LIBs within 1.2–4.3 V. The cyclic voltammetry (CV) curve of BT-COF exhibits three pairs of redox peaks at 2.0 (O1)/1.3 V (R1), 3.3 (O2)/2.2 V (R2), and 4.0 (O3)/3.8 V (R3), as shown in Fig. 3a, which represent cation storage at BTT carbons, cation insertion into imine and formyl groups based on similar redox voltages, and anion storage in TPA and BTT units.[37] In contrast, BT-COF/CNT-50 retains three pairs of redox peaks with narrower voltage gaps at 2.2/1.3 V, 3.3/2.2 V, and 4.0/3.7 V, indicating improved reversibility arising from improved electrical conductivity based on π–π interfacial interactions with CNTs. RBT-COF@CNT-50 also displays three pairs of redox peaks, including 2.0 (O1)/1.6 V (R1), 3.0 (O2)/2.5 V (R2), and 4.0 (O3)/3.8 V (R3) (Fig. 3a). Meanwhile, three pairs of redox peaks for RBT-COF@CNT-50 show further narrower voltage gaps, especially for the redox peak (O2/R2) for cation insertion into imine and formyl groups, which shows a larger peak area. These phenomena indicate that the curvature defect engineering is conducive to promoting ion storage with better reaction activity. The O1 peak is relatively weak because of the sluggish ion-release process occurring within the lower-voltage region, which resembles the intercalation behavior observed in graphene.[16] Moreover, unlike the cations coordinated within the BTT units (O1/R1), cations stored at the imine and unreacted aldehyde experience stronger binding interactions as supported by the ESP analysis in Fig. 2b. Consequently, Li^+ extraction from these sites requires a higher redox voltage, giving rise to the O2/R2 peaks with more pronounced current responses.[38] The CV curves of RBT-COF@CNT-10 and RBT-COF@CNT-30 exhibited similar characteristics, as shown in Fig. S10. The integrated CV area of RBT-COF@CNT-50 is 1.3 and 1.2 times greater than those of BT-COF and BT-COF/CNT-50, respectively, highlighting enhanced redox kinetics and more accessible active sites enabled by curvature defect engineering.[39] The charging and discharging curves at 0.1 A g^{-1} (Fig. 3b) corroborate the CV results. RBT-COF@CNT-50 exhibits a discharge plateau at 1.4 V, corresponding to Li^+ storage at BTT, and two additional plateaus at ∼2.5 and ∼3.8 V, associated with Li^+ insertion into imine/formyl groups and PF_6^- release from TPA/BTT, respectively.[16] Notably, the ∼2.5 V plateau is not obvious in BT-COF and BT-COF/CNT-50, underscoring that defects in RBT-COF facilitate the reversible utilization of otherwise less accessible redox sites. Furthermore, the voltage gap significantly reduces from 0.87 V for BT-COF and 0.76 V for BT-COF/CNT-50 to 0.48 V for RBT-COF@CNT-50, indicating suppressed polarization due to curvature defect engineering.

The cycling performance at 0.1 A g^{-1} (Fig. 3c) demonstrates that RBT-COF@CNT-50 maintains a high specific capacity of 388 mAh g^{-1} after 100 cycles, outperforming BT-COF (195 mAh g^{-1}) and BT-COF/CNT-50 (130 mAh g^{-1}). The initial decrease in capacity can be attributed to the formation of the cathode electrolyte interphase (CEI).[16] The following activated process may be attributed to the gradually alleviated tight stacking between the framework.[8] In addition, the first and second-cycle charge/discharge curves of RBT-COF@CNT-50 at 0.1 A g^{-1} are displayed in Fig. S11. The initial coulombic efficiency (CE) of RBT-COF@CNT-50 is 60%, which is attributed to the CEI formation with the extra lithium-ion intercalation during the first discharge process at a lower-voltage range.[8] The CE in the second-cycle can reach 89%, which is comparable to commercialized inorganic cathode materials.[40,41] Although the major capacity contribution originates from the n-type region in RBT-COF@CNT-50, designing a D–A COF with more p-type redox active sites may be a good solution to increase capacity in the high voltage range.[6] The distinct redox peaks can be well-retained over cycling in differential capacity (dQ/dV) analysis (Fig. 3d), further indicating stable redox reversibility with high active-site utilization. Rate performance testing (Fig. 3e) reveals the superior kinetics of RBT-COF@CNT-50. At 0.1 A g^{-1}, it delivers 300 mAh g^{-1}, markedly higher than BT-COF (156 mAh g^{-1}) and BT-COF/CNT-50 (171 mAh g^{-1}). Even at increased current densities of 0.3, 0.5, 1, 2, 5, and 10 A g^{-1}, RBT-COF@CNT-50 still maintains 255, 219, 177, 145, 112, and 88 mAh g^{-1}, respectively, and readily recovers capacities of 158, 214, and 302 mAh g^{-1} when the current densities are returned to 2, 0.5, and 0.1 A g^{-1}. In comparison, BT-COF and BT-COF/CNT-50 show lower specific capacity at each current density, as shown in Fig. 3e. It should be mentioned that the reason for the rapid capacity decay with increasing current density in RBT-

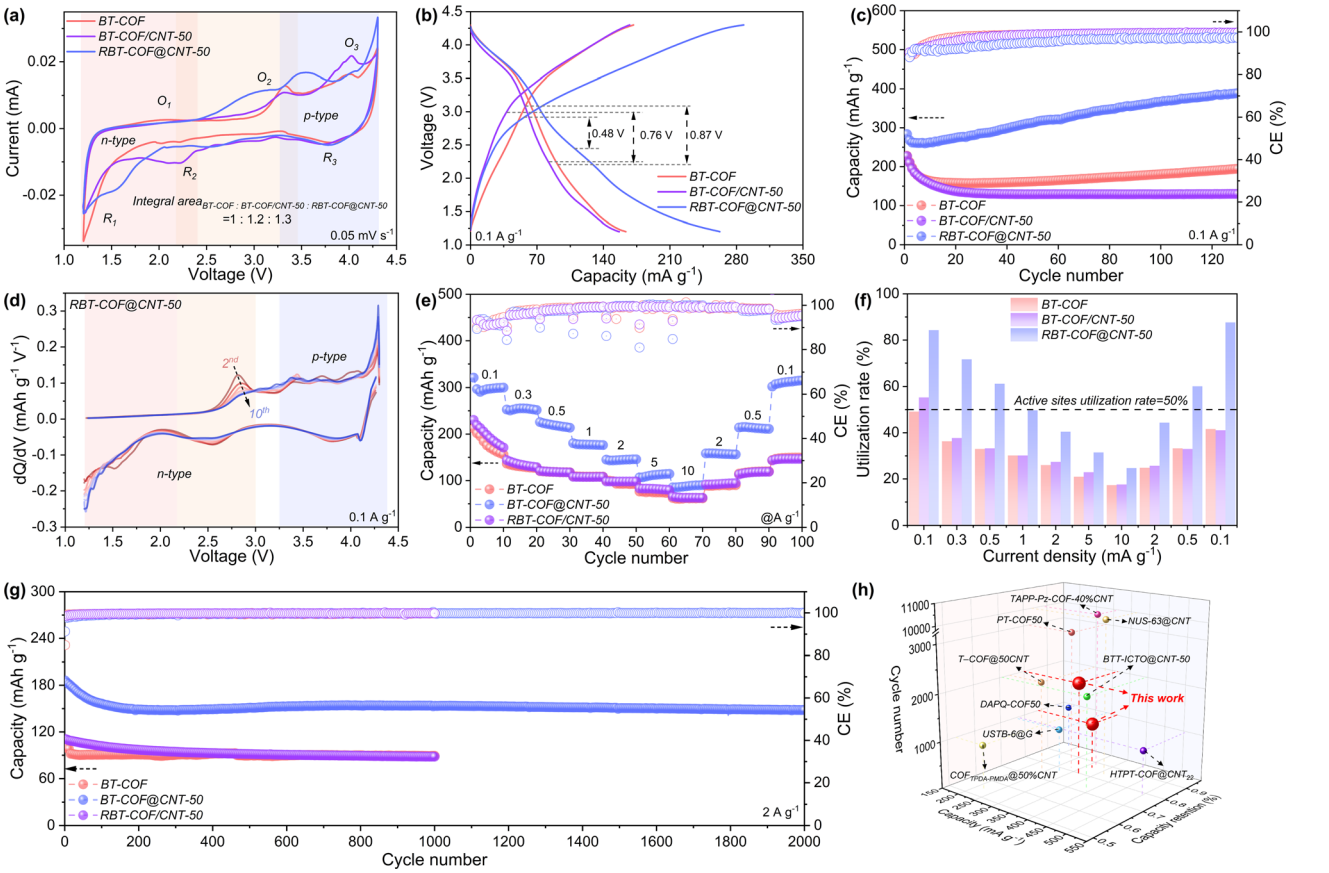

Fig. 3 (a) CV curves at 0.05 mV s^{-1}, (b) charging and discharging curves, and (c) cycle performance at 0.1 A g^{-1} for BT-COF, BT-COF/CNT-50, and RBT-COF@CNT-50. (d) dQ/dV curves for RBT-COF@CNT-50. (e) Rate performance, (f) active-site utilization rates, and (g) long-term cycling performance at 2 A g^{-1} for BT-COF, BT-COF/CNT-50, and RBT-COF@CNT-50. (h) Comparison of electrochemical performance for RBT-COF@CNT-50 with recently reported COF/carbon composite cathode materials.

COF@CNT-50 is the exacerbation of concentration polarization.[42,43] Active-site utilization rates (Fig. 3f) further highlight the advantage of RBT-COF@CNT-50 with 88% theoretical capacity calculated by eqn (S2) at 0.1 A g^{-1}, while BT-COF and BT-COF/CNT-50 exhibit only 49% and 55%, respectively. Long-term cycling at 2 A g^{-1} (Fig. 3g) demonstrates the durability of RBT-COF@CNT-50, which delivers 148 mAh g^{-1} after 2000 cycles, significantly higher than BT-COF (89 mAh g^{-1}) and BT-COF/CNT-50 (88 mAh g^{-1}) after 1000 cycles. In contrast to the cycle performance at 0.1 A g^{-1}, the capacity of all samples will show a gradual decrease followed by stabilization caused by the high concentration polarization at high current density.[42,43] Even under an ultrahigh current density of 10 A g^{-1}, RBT-COF@CNT-50 retains a high initial discharge capacity of 124 mAh g^{-1} with an ultralow fading rate of 0.004% per cycle, as shown in Fig. S12. The electrochemical performances of RBT-COF@CNT-10 and RBT-COF@CNT-30 were also measured, as shown in Fig. S13. Finally, the comprehensive performance of RBT-COF@CNT-50 surpasses that of the reported COF/carbon composite cathodes[15,22,44–50] in terms of capacity, retention, and cycling stability in Fig. 3h, which can be attributed to its optimized electron pathways and accelerated ion diffusion for efficient utilization of redox-active sites.

The ion diffusion behavior was further evaluated through electrochemical reaction kinetics. As shown in Fig. 4a and S14, CV curves at different scan rates (0.2–1.0 mV s^{-1}) were recorded to investigate the ion storage behavior. For BT-COF (Fig. S14a), the oxidation peak at ~3.3 V gradually disappears at scan rates above 0.6 mV s^{-1}. In contrast, the reversible redox peaks O1 (~3.0 V) and R1 (~2.4 V) remain clearly observable even at 1.0 mV s^{-1} for BT-COF/CNT-50 and RBT-COF@CNT-50 (Fig. S14b and a), which can be attributed to enhanced active site accessibility enabled by the superior electron transport of CNTs. A similar trend is also observed for RBT-COF@CNT-10 and RBT-COF@CNT-30 (Fig. S14c and d). The fitted b-values of O1, O2, R1, and R2 are approximately 0.7 based on eqn (S3) in Fig. S15, indicating that the charge storage process is predominantly diffusion-controlled.[51] The capacitive contribution was further quantified by separating surface-controlled and diffusion-controlled capacitances using eqn (S4) (Fig. 4b). For BT-COF and BT-COF/CNT-50, the surface-controlled contribution increases from 65% and 73% at 0.2 mV s^{-1} to 89% and 93% at 1.0 mV s^{-1}, respectively. In contrast, RBT-COF@CNT-50 consistently exhibits a higher diffusion-controlled contribution, with the pseudocapacitance increasing from 54% to 70% as the scan rate increases. The increased diffusion-controlled

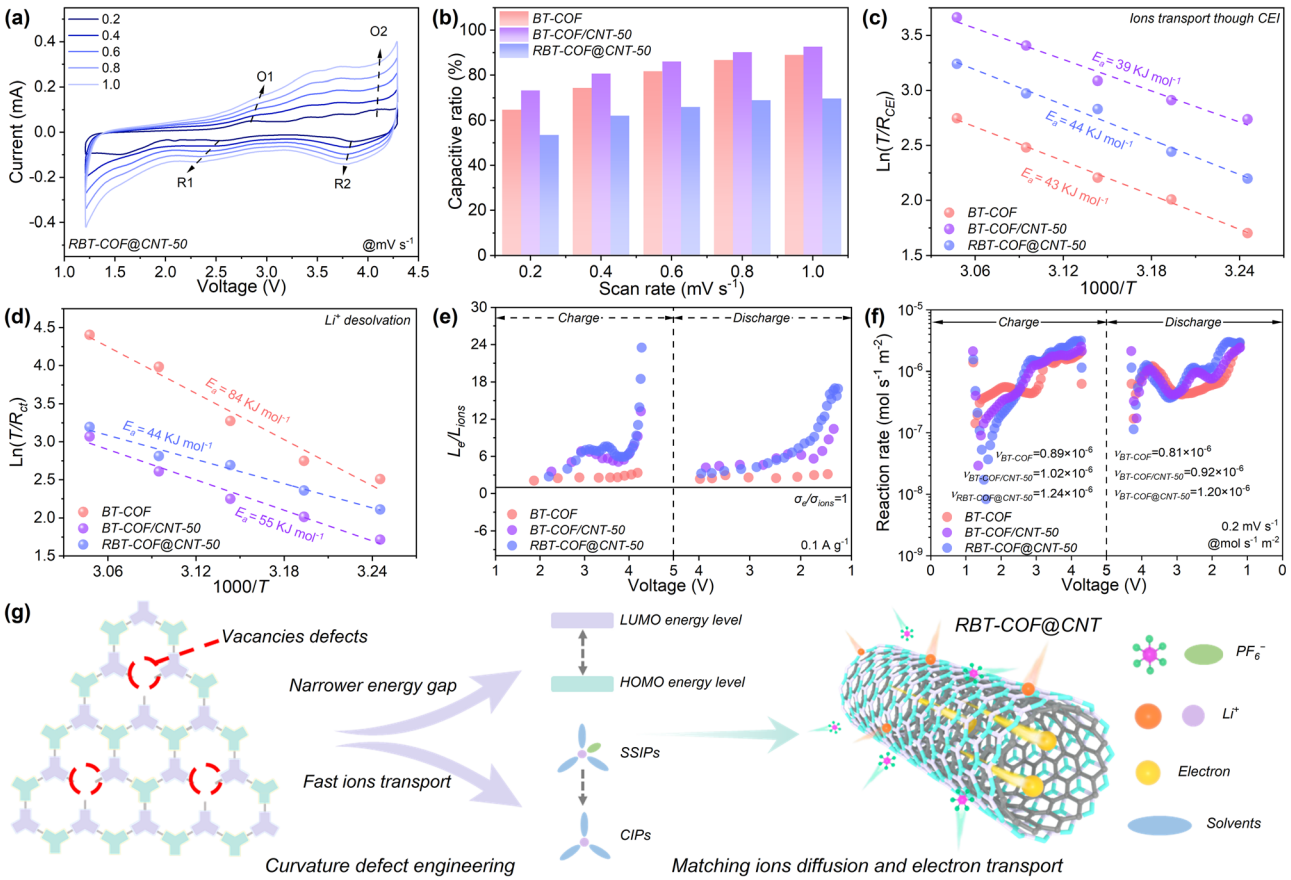

Fig. 4 (a) CV curves at various scan rates for RBT-COF@CNT-50. (b) Contribution ratios of the surface-controlled capacitances for BT-COF, BT-COF/CNT-50, and RBT-COF@CNT-50. The diffusion activation energy of (c) Li^+ transport through the CEI and (d) Li^+ desolvation for BT-COF, BT-COF/CNT-50, and RBT-COF@CNT-50. (e) The Le/Lions values and (f) reaction rates for BT-COF, BT-COF/CNT-50, and RBT-COF@CNT-50. (g) A schematic diagram showing matching ion diffusion and electron transport by curvature defect engineering.

contribution may result from the shortened ion diffusion pathways due to the incorporation of CNTs. This demonstrates that curvature defect engineering is conducive to ion diffusion, retaining high intrinsic pseudocapacitance.

The enhanced accessibility of active sites was further examined by activation energy (E_a) analysis based on electrochemical impedance spectroscopy (EIS) at various temperatures (Fig. S16). The distribution of relaxation times (DRT) method was employed, along with three regions assigned τ_1 to τ_5, *i.e.*, τ_1 corresponding to contact resistance, τ_2 and τ_3 corresponding to interfacial resistance, and τ_4 and τ_5 representing charge transfer resistance (Fig. S17 and Table S2).[52,53] Notably, both interfacial and charge transfer resistances are significantly reduced for RBT-COF@CNT-50, confirming that the defect engineering facilitates electron transport by introducing electron-withdrawing aldehyde groups based on the CNT conductive network. The E_a was further calculated to distinguish between ion transport across the CEI, as shown in Fig. 4c, and the Li^+ desolvation process shown in Fig. 4d based on eqn (S5).[54] The E_a for Li^+ desolvation in RBT-COF@CNT-50 is lowest at 44 kJ mol^{-1}, in contrast to BT-COF (84 kJ mol^{-1}) and BT-COF/CNT-50 (55 kJ mol^{-1}), while the E_a for ion transport through the CEI is comparable to that of BT-COF. This result indicates accelerated ion dissociation with faster reaction kinetics in RBT-COF@CNT-50 as a result of curvature defect engineering.

The faster electrochemistry reaction kinetics were further analyzed based on the "wings length" concept.[10] The σ_e of the electrode slurries was measured as 0.91 × 10^{-3}, 2.25 × 10^{-3}, and 1.37 × 10^{-3} S m^{-1} for BT-COF, BT-COF/CNT-50, and RBT-COF@CNT-50, respectively, as shown in Fig. S18. The higher σ_e of RBT-COF@CNT-50 relative to BT-COF is attributed to the synergistic effect of more defects and π–π interactions between CNTs and the COF backbone. The ion conductivity (σ_{ions}) was evaluated using the galvanostatic intermittent titration technique (GITT, Fig. S19) based on Fick's law (eqn (S6)) and the Nernst–Einstein relation (eqn (S7)). Interestingly, the average σ_{ions} of RBT-COF@CNT-50 (0.18 × 10^{-3} S m^{-1}) are lower than that of BT-COF (1.23 × 10^{-3} S m^{-1}) and comparable to BT-COF/CNT-50 (0.22 × 10^{-3} S m^{-1}). The reduced D_{ions} with increasing CNT content likely arise from internal CNT encapsulation during polymerization, which hinders effective ion diffusion. In addition, the low D_{ions} of BT-COF/CNT-50 may also be because of the spatial hindrance effect based on the π–π interactions between CNTs and the COF backbone. Nevertheless, TEM analysis confirms that a thinner COF coating layer forms on the CNT surface with increasing CNT content, thereby shortening

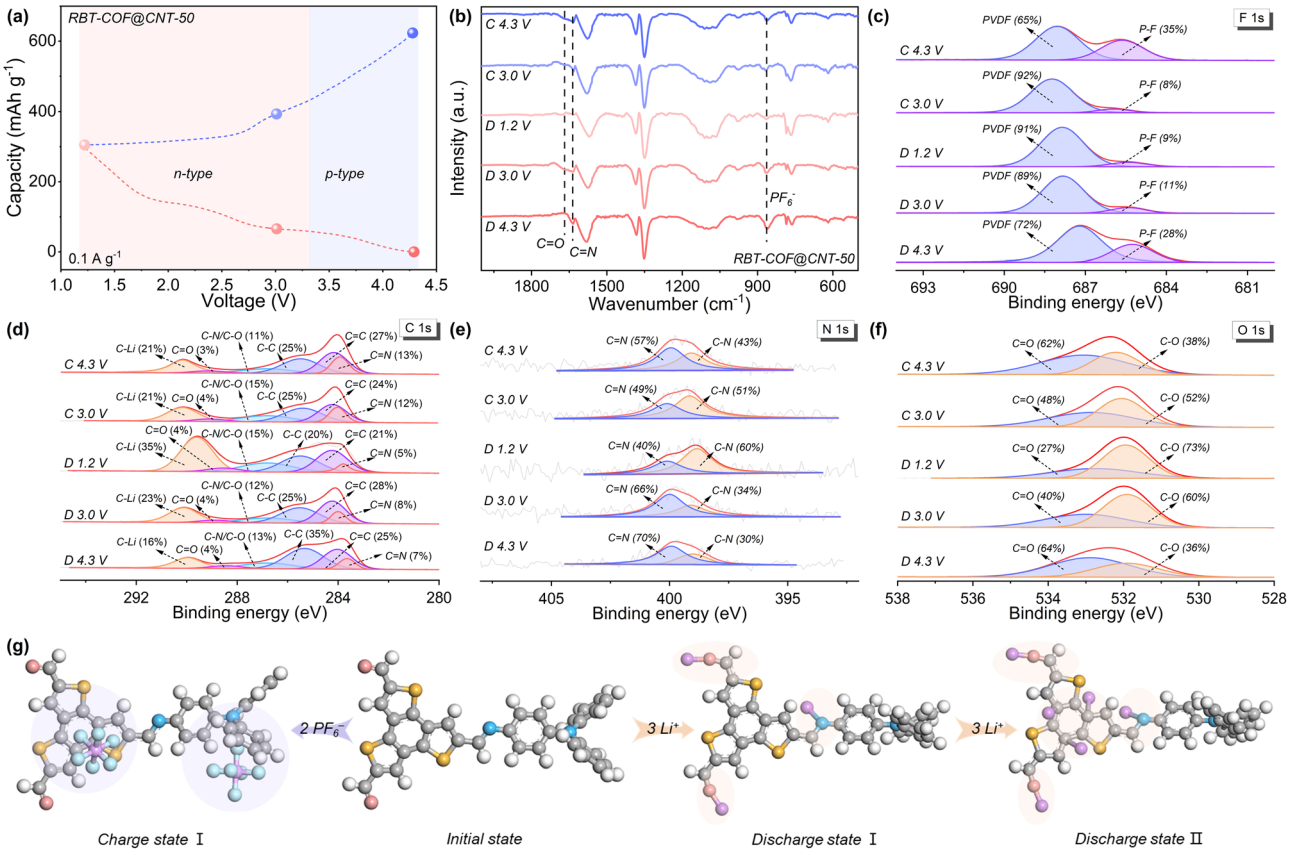

Fig. 5 (a) The charge–discharge curve of the RBT-COF@CNT-50 electrode at 0.1 A g^{-1} for pristine and selected redox states. (b) The *ex situ* FT-IR spectra, and (c) F 1s, (d) C 1s, (e) N 1s, and (f) O 1s XPS spectra of RBT-COF@CNT-50. (g) DFT calculation of the reaction mechanism during the bipolar storage process in the BT-COF model on the surface of CNTs.

ion diffusion pathways and synergistically coupling fast electron transport in RBT-COF@CNT-50.

/The calculated L_e/L_{ions} values (Fig. 4e) show that those of both BT-COF/CNT-50 and RBT-COF@CNT-50 exceed that of BT-COF at 0.1 A g^{-1}. However, as the electrochemical reactions ultimately rely on active sites within the COF framework, the σ_e of the active material plays a decisive role in determining site utilization. Indeed, the σ_e of BT-COF is much lower than that of RBT-COF@CNT-50, resulting in limited active site accessibility for BT-COF. This is further confirmed by calculating σ_e/σ_{ions} (Fig. S20). Consistently, reaction rate (v) analysis based on Faraday's law (eqn (S8)–(11), Fig. 4f) shows an enhancement from 0.85 × 10^{-6} mol s^{-1} m^{-2} (BT-COF) to 0.97 × 10^{-6} (BT-COF/CNT-50) and 1.22 × 10^{-6} mol s^{-1} m^{-2} (RBT-COF@CNT-50). To better demonstrate the innovativeness of RBT-COF@CNT-50, a schematic diagram for matching ion diffusion and electron transport by curvature defect engineering is shown in Fig. 4g. With curvature defect engineering, more vacancy defects emerge with CNTs, which is beneficial to obtain a narrower energy gap and fast ion diffusion for matching ion diffusion and electron transport, achieving better electrochemical reaction kinetics. It should be noted that the gradually decreased S_{BET} with lower pore accessibility (pore volume) can be observed, accompanied by increasing CNT addition proportion, as shown in Table S3. This observation may be attributed to more polymerization sites and substrate curvature-induced effect of CNTs, weakening interlayer stacking and generating relative slipping, resulting in low D_{ions}.[15,24] Therefore, although BT-COF displays higher S_{BET} with better pore accessibility and D_{ions}, the agglomeration morphology of COF nanocrystals still limits the efficient utilization of their active sites.[55]

To gain deeper insights into the charge storage mechanism, *ex situ* FT-IR and XPS measurements were conducted to monitor structural changes of RBT-COF@CNT-50 at selected voltages, based on the proposed bipolarization reaction mechanism with different discharge platforms discussed above (Fig. 5a). As shown in Fig. 5b, the stretching vibrations of C=O (1669 cm^{-1}) and C=N (1634 cm^{-1}) progressively weaken as the voltage decreases from 4.3 to 1.2 V during discharging. Upon recharging to 3.0 V, both C=O and C=N peaks reappear, indicating an n-type reaction associated with Li^+ insertion and the formation of C–O–Li and C–N–Li bonds.[16,37] At higher voltages up to 4.3 V, the peak corresponding to PF_6^- (864 cm^{-1}) becomes more pronounced, consistent with a p-type reaction involving anion coordination.[8,16] These observations are corroborated by the F 1s XPS spectra (Fig. 5c), where the characteristic P–F peak (685 eV) remains dominant at high voltage but gradually decreases upon discharging. The C 1s XPS spectra (Fig. 5d) further verify the n-type process. The proportion of C–Li (290 eV) increases significantly from 16% to 35% during discharging, partially recovering to 21% upon charging. Concurrently, the proportion

of C–N/C–O increases from 13% to 15%, confirming that both C═O and C═N groups serve as redox-active sites during Li^+ insertion. Additional evidence from N 1s and O 1s spectra (Fig. 5e and f) further supports these functional group transformations. Notably, the C═C proportion decreases from 28% to 21%, suggesting that certain C═C bonds within the BTT units also participate in Li^+ binding, contributing to the enhanced capacity.

Based on these observations and supported by DFT calculations, a three-stage charge storage mechanism is proposed in Fig. 5g. (1) Charge state (p-type reaction): the BTT and TPA units act as active sites for the storage of two anions above 3.0 V, with a Gibbs free energy (ΔG) of −0.5 eV. (2) Discharge state I (n-type reaction): three Li^+ ions are accommodated in two aldehyde groups and one imine bond of the framework, with ΔG of −4.6 eV. (3) Discharge state II: an additional three Li^+ ions are stored at carbon sites of BTT, yielding a lower ΔG of −11.6 eV, validating the proposed binding-site model. All results based on the *ex situ* spectra analyses and DFT calculations provide compelling evidence that the superior capacity of RBT-COF@CNT-50 originates from its bipolarization-driven charge storage mechanism.

Conclusions

In summary, we propose a defect-rich COF@CNT cathode (RBT-COF@CNT) generated by curvature defect engineering to optimize electron transport and ion diffusion through a one-pot Schiff-base reaction with CNTs as templates. With the help of multiple electron transport enhancement based on a defect-rich D–A system with a CNT-interlaced network, RBT-COF@CNT achieves an excellent electron conductivity of 2.65×10^{-4} S m^{-1}. Benefitting from the emergence of more polar functional groups originating from defects, RBT-COF@CNT achieves faster ion dissociation and a higher reaction rate of 1.22×10^{-6} mol s^{-1} m^{-2}. As expected, RBT-COF@CNT-50 reveals a high specific capacity of 302 mAh g^{-1} at 0.1 A g^{-1}, good long-term cycling performance with 148 mA g^{-1} at 2 A g^{-1} for 2000 continuous cycles, and low capacity attenuation rate of 0.004% per cycle at 10 A g^{-1}, outperforming most reported COF/carbon composite cathodes. This work provides a valuable reference for designing a porous nanofiber cathode with high-performance by synchronously optimizing electron transport and ion diffusion.

Author contributions

W. L. and Y. Z. L. conceived the project. J. D., H. J. Z., and X. Y. S. synthesized the samples, performed the structural characterizations, and implemented structural simulations. J. D., W. X. B., and J. W. L. participated in the electrochemical tests. L. C. X. conducted DFT theoretical calculations. W. S. H. and H. W. H. performed the formatting of the manuscript. All authors analyzed the results and commented on the manuscript.

Conflicts of interest

There are no conflicts of interest to declare.

Data availability

The data supporting this article have been included as part of the supplementary information (SI). Supplementary information: the text of experimental section and characterization, the supplied equations, the supplied figures of structural and morphological characterization, electrochemical performance, solvent-structured characterization, ionic diffusion kinetics, and the σ_e/σ_{ions} values, and the supplied tables. See DOI: https://doi.org/10.1039/d5sc07537h.

Acknowledgements

The authors thank for financial support the Shanghai Science and Technology Plan Project (25DX1400200), the National Natural Science Foundation of China (52373172, and 52473055), the Key Technology Research and Development Program of Shanghai (25CL2900800), the Chang Jiang Scholar Program (T2023082), the Natural Science Foundation of Shanghai (23ZR1401100), and the Fundamental Research Funds for the Central Universities (CUSF-DH-D-2025003).

References

1 T. Jiang, D. Shen, Z. Zhang, H. Liu, G. Zhao, Y. Wang, S. Tan, R. Luo and W. Chen, *Nat. Rev. Clean Technol.*, 2025, **1**, 474–492.
2 Y. Xu, L. Jiao, J. Ma, P. Zhang, Y. Tang, L. Liu, Y. Liu, H. Ding, J. Sun, M. Wang, Z. Li, H.-L. Jiang and W. Chen, *Joule*, 2023, **7**, 515–528.
3 A. Mahmood, Z. Bai, T. Wang, Y. Lei, S. Wang, B. Sun, H. Khan, K. Khan, K. Sun and G. Wang, *Chem. Soc. Rev.*, 2025, **54**, 2369–2435.
4 Y. Xu, M. Wang, M. Sajid, Y. Meng, Z. Xie, L. Sun, J. Jin, W. Chen and S. Zhang, *Angew. Chem., Int. Ed.*, 2024, **63**, e202315931.
5 M. Zheng, X. Zhu, H. Zheng, Z. Bo and J. Lu, *Nat. Energy*, 2025, **10**, 789–792.
6 K. Amin, B. C. Baker, L. Pan, W. Mehmood, Z. Hao, R. Nawaz, Z. Wei and C. F. J. Faul, *Adv. Mater.*, 2025, **37**, 2410262.
7 A. L. Waentig, X. Li, M. Zhao, S. Haldar, P. Koko, S. Paasch, A. Mueller, K. M. G. Alvarez, F. Auras, E. Brunner, A. Schneemann, J.-Q. Huang, S. Kaskel, M. Wang and X. Feng, *Chem. Sci.*, 2025, **16**, 4152–4158.
8 J. Duan, K. Wang, L. Teng, H. Liu, L. Xu, Q. Huang, Y. Li, M. Liu, H. Hu, X. Chen, J. Wang, W. Yan, W. Lyu and Y. Liao, *ACS Nano*, 2024, **18**, 29189.
9 L. Zhu, Y. Cao, T. Xu, H. Yang, L. Wang, L. Dai, F. Pan, C. Chen and C. Si, *Energy Environ. Sci.*, 2025, **18**, 5675–5739.
10 C. Zhu, R. E. Usiskin, Y. Yu and J. Maier, *Science*, 2017, **358**, eaao2808.
11 J. Zheng, R. Garcia-Mendez and L. A. Archer, *ACS Nano*, 2021, **15**, 19014–19025.
12 Y. Li, J. Duan, Y. Wang, L. Teng, H. Liu, J. Li, M. Liu, W. He, H. Hu, L. Wang, W. Lyu and Y. Liao, *Chem. Sci.*, 2025, **16**, 11311–11321.

13 X. Xu, S. Zhang, K. Xu, H. Chen, X. Fan and N. Huang, *J. Am. Chem. Soc.*, 2023, **145**, 1022–1030.
14 L. Guo, L. Gong, Y. Yang, Z. Huang, X. Liu and F. Luo, *Angew. Chem., Int. Ed.*, 2025, **64**, e202414658.
15 L. Yao, C. Ma, L. Sun, D. Zhang, Y. Chen, E. Jin, X. Song, Z. Liang and K.-X. Wang, *J. Am. Chem. Soc.*, 2022, **144**, 23534–23542.
16 J. Duan, F. Chen, H. Yu, S. Zhu, L. Teng, K. Wang, T. Chen, W. Lyu, H. Hu and Y. Liao, *Angew. Chem., Int. Ed.*, 2025, **64**, e202505207.
17 G. Lai, J. Lin, W. Mo, X. Li, X. Jin, M. Wu and F. Liu, *J. Am. Chem. Soc.*, 2025, **147**, 13071–13081.
18 Z. Jiang, M. Pang, C. Luo, Z. Yao, T. Fu, T. Pan, W. Sun, Y. Li, Q. Guo, S. Xiong, C. Zheng, G. Zhou and S. Liu, *Energy Storage Mater.*, 2024, **72**, 103729.
19 W. Deng, G. Li and X. Wang, *Adv. Funct. Mater.*, 2024, **34**, 2405012.
20 K. Du, L. Xiong, C. Fu, X. Ni, J.-L. Bredas and H. Li, *ACS Mater. Lett.*, 2024, **6**, 335–344.
21 Z. Guo, H. Wu, Y. Chen, S. Zhu, H. Jiang, S. Song, Y. Ren, Y. Wang, X. Liang, G. He, Y. Li and Z. Jiang, *Angew. Chem., Int. Ed.*, 2022, **61**, e202210466.
22 Q. Xu, Z. Liu, Y. Jin, X. Yang, T. Sun, T. Zheng, N. Li, Y. Wang, T. Li, K. Wang and J. Jiang, *Energy Environ. Sci.*, 2024, **17**, 5451–5460.
23 J. He, Y. Zhao, Y. Li, Q. Yuan, Y. Wu, K. Wang, K. Sun, J. Wu, J. Jiang, B. Zhang, L. Wang and M. Fan, *Nano-Micro Lett.*, 2025, **17**, 221.
24 D. Jiang, R. Xu, L. Bai, J. P. Hill, J. Henzie, L. Zhu, W. Xia, R. Bu, Y. Zhao, Y. Kang, T. Hamada, R. Ma, N. Torad, J. Wang, T. Asahi, X. Xu and Y. Yamauchi, *Adv. Funct. Mater.*, 2024, **34**, 2407479.
25 B. A. Atterberry, P. Paluch, A. R. Lamkins, W. Huang and A. J. Rossini, *J. Am. Chem. Soc.*, 2025, **147**, 14411–14421.
26 Y. Xie, S. Wu, Z. Zhu, J. Wang, Z. Kuang, L. Zhang, A. Abdurahman, Q. Peng and X. Ai, *Angew. Chem., Int. Ed.*, 2025, **64**, e202515346.
27 S. Kang, Y. Jiang, Y. Shi, X. Lou, F. Geng and B. Hu, *Chem. Mater.*, 2024, **36**, 4092–4106.
28 J. Liu, Q. Guo, H. Tian, Y. Cheng, X. Xu, Z. Zhang, H. Hao, Z. Ding, K. Jiao, J. Zheng, J. Zhang and X. Gao, *Matter*, 2025, **8**, 102427.
29 Y. Zhang, M. Chen, X. He, E. Zhao, H. Liang, J. Shang, K. Liu, J. Chen, S. Zuo and M. Zhou, *Nat. Commun.*, 2025, **16**, 2652.
30 Q. Li, D.-D. Ma, W.-B. Wei, S.-G. Han, L. Zheng and Q.-L. Zhu, *Adv. Energy Mater.*, 2024, **14**, 2401314.
31 Z. Lei, Q. Yang, Y. Xu, S. Guo, W. Sun, H. Liu, L.-P. Lv, Y. Zhang and Y. Wang, *Nat. Commun.*, 2018, **9**, 576.
32 W. Yuan, J. Weng, M. Ding, H.-M. Jiang, Z. Fan, Z. Zhao, P. Zhang, L.-P. Xu and P. Zhou, *Energy Storage Mater.*, 2023, **65**, 103142.
33 Y. Zhuang, H. Yang, Y. Li, Y. Zhao, H. Min, S. Cui, X. Shen, H.-Y. Chen, Y. Wang and J. Wang, *ACS Nano*, 2025, **19**, 11058–11074.
34 C. Liu, X. Huang, X. Yu, Z. Wang, Y. Shen, S. Yuan and Y. Wang, *Angew. Chem., Int. Ed.*, 2025, **64**, e202415915.
35 D.-H. Guan, X.-X. Wang, L. Li, G.-N. Chen, G.-Y. Qiao and J.-J. Xu, *J. Am. Chem. Soc.*, 2025, **147**, 38078–38088.
36 C. Zhou, Y. Zhou, S. Hao, G. Li, S. Liu and X. Gao, *Cell Rep. Phys. Sci.*, 2024, **5**, 101999.
37 Q. Bai, J. Huang, K. Tang, Y. Zhu and D. Wu, *Adv. Mater.*, 2025, **37**, 2416661.
38 S. Zheng, D. Shi, T. Sun, L. Zhang, W. Zhang, Y. Li, Z. Guo, Z. Tao and J. Chen, *Angew. Chem., Int. Ed.*, 2023, **62**, e202217710.
39 J. Duan, W. Wang, D. Zou, J. Liu, N. Li, J. Weng, L.-P. Xu, Y. Guan, Y. Zhang and P. Zhou, *ACS Appl. Mater. Interfaces*, 2022, **14**, 31234–31244.
40 Z. Li, Y. Wang, J. Wang, C. Wu, W. Wang, Y. Chen, C. Hu, K. Mo, T. Gao, Y.-S. He, Z. Ren, Y. Zhang, X. Liu, N. Liu, L. Chen, K. Wu, C. Shen, Z.-. Ma and L. Li, *Nat. Commun.*, 2024, **15**, 10216.
41 P. Yang, L. Shang, H. Wang, Z. Yan, K. Zhang, Y. Li and J. Chen, *Angew. Chem., Int. Ed.*, 2025, **64**, e202501539.
42 J. Duan, L. Teng, H. Liu, X. Zhang, H. Yu, Q. Huang, Y. Li, M. Liu, H. Hu, W. Lyu and Y. Liao, *Angew. Chem., Int. Ed.*, 2025, **64**, e202517853.
43 C. Song, S. H. Han, Y. Choi, H. R. Shin, M. K. Kim, C. Gong, D. Chen, J.-W. Lee, S. Hong and N.-S. Choi, *Adv. Mater.*, 2025, **37**, 2418773.
44 H. Gao, A. R. Neale, Q. Zhu, M. Bahri, X. Wang, H. Yang, Y. Xu, R. Clowes, N. D. Browning, M. A. Little, L. J. Hardwick and A. I. Coope, *J. Am. Chem. Soc.*, 2022, **144**, 9434–9442.
45 N. Fu, Y. Liu, K. Kang, X. Tang, S. Zhang, Z. Yang, Y. Wang, P. Jin, Y. Niu and B. Yang, *Angew. Chem., Int. Ed.*, 2024, **63**, e202412334.
46 Y. Wang, J. Wang, J. Peng, Y. Jiang, Y. Zhu and Y. Yang, *ACS Nano*, 2024, **18**, 23958–23967.
47 W. Li, Q. Huang, H. Shi, W. Gong, L. Zeng, H. Wang, Y. Kuai, Z. Chen, H. Fu, Y. Dong and C. Zhang, *Adv. Funct. Mater.*, 2024, **34**, 2310668.
48 C. Jia, A. Duan, C. Liu, W.-Z. Wang, S.-X. Gan, Q.-Y. Qi, Y. Li, X. Huang and X. Zhao, *Small*, 2023, **19**, 2300518.
49 S. Biswas, A. Pramanik, A. Dey, S. Chattopadhyay, T. S. Pieshkov, S. Bhattacharyya, P. M. Ajayan and T. K. Maji, *Small*, 2024, **20**, 2406173.
50 X. Liu, Y. Jin, H. Wang, X. Yang, P. Zhang, K. Wang and J. Jiang, *Adv. Mater.*, 2022, **34**, 2203605.
51 H. Gao, Q. Zhu, A. R. Neale, M. Bahri, X. Wang, H. Yang, L. Liu, R. Clowes, N. D. Browning, R. S. Sprick, M. A. Little, L. J. Hardwick and A. I. Cooper, *Adv. Energy Mater.*, 2021, **11**, 2101880.
52 W. Ma, Y. Guo, J. Sun, C. Zhang, Y. Zhu, H. Sun, L. Huang, Z. Hu, H. Wang, M. Zhu and G. Wang, *Angew. Chem., Int. Ed.*, 2025, **64**, e202418999.
53 Y. Lu, C. Z. Zhao, J. Q. Huang and Q. Zhang, *Joule*, 2022, **6**, 1172–1198.
54 X. Yin, B. Li, H. Liu, B. Wen, J. Liu, M. Bai, Y. Zhang, Y. Zhao, X. Cui, Y. Su, G. Gao, S. Ding and W. Yu, *Joule*, 2025, **9**, 101823.
55 R. Wan, T. Yuan, L. Wang, B. Li, M. Liu and B. Zhao, *Nat. Catal.*, 2024, **7**, 1288–1304.